Available online at www.sciencedirect.com
SCIENCE DIRECT®
Journal of Computational Physics 206 (2005) 252–276
JOURNAL OF COMPUTATIONAL PHYSICS
www.elsevier.com/locate/jcp

A 2D compact fourth-order projection decomposition method

Stéphane Abide, Stéphane Viazzo *

Ecole des Mines de Nantes, GEPEA, UMR CNRS 6144, 4 Rue Alfred Kastler, BP 20722 44307, Nantes Cedex 03, France

Received 16 August 2004; received in revised form 7 December 2004; accepted 7 December 2004
Available online 22 January 2005

Abstract

A 2D fourth-order compact direct scheme projection decomposition method for solving incompressible viscous flows in multi-connected rectangular domains is devised. In each subdomain, the governing Navier–Stokes equations are discretized by using fourth-order compact schemes in space and second-order scheme in time. The coupling between subdomains is based on a direct non-overlapping multidomain method: it allows to solve each Helmholtz/Poisson problem resulting of a projection method in complex geometries. The major difficulty of the Poisson–Neumann problem solvability is addressed and correctly treated. The present numerical method is checked through some classical numerical experiments. First, the second-order accuracy in time and the fourth-order accuracy in space are shown by matching with the analytical solution of the Taylor problem. The method is also tested by simulating the flow in a 2D lid-driven cavity. The utility of the compact scheme projection decomposition method approach is further illustrated by two other benchmark problems, viz., the flow over a backward-facing step and the laminar flow past a square prism. The present results are in good agreement with the experimental data and other numerical solutions available in the literature.

Keywords: Domain decomposition method; Compact scheme; Projection scheme

1. Introduction

Many physical process exhibit a wide range of space and time scales which may be numerically computed. This requirement has led to the development of highly accurate schemes like spectral methods or compact schemes. A relevant framework is the turbulence research area, in which the range of the physical space and time scales increases with the Reynolds number. In this context, spectral methods or compact

* Corresponding author. Tel.: +33 2 51 85 82 91; fax: +33 2 51 85 82 99.
E-mail address: stephane.viazzo@emn.fr (S. Viazzo).

0021-9991/$ - see front matter © 2005 Elsevier Inc. All rights reserved.
doi:10.1016/j.jcp.2004.12.005

schemes have been intensively used in various way such as direct numerical simulation or large eddy simulation. However, these methods are limited to flows in rectangular computational domains with simple boundary conditions. Some works showed that domain decomposition could be an efficient method to simulate turbulent flows in complex geometries defined by multi-connected rectangular domains [1–3]. This work focuses on a 2D compact scheme projection decomposition method (PDM) applied to the numerical simulation of 2D incompressible laminar flows. The pressure-velocity formulation has been selected for its ability to simulate three-dimensional turbulent flows with one periodic direction [2].

Compact finite difference schemes achieve high order accuracy and good resolution properties without increasing excessively the computational stencil size. Several authors [4,5] contributed to the development of these schemes. Recently, they are again coming in use in derived forms, depending on applications: finite differences or finite volumes [6–13]. Various successful works, based on compact schemes, include DNS and LES of classical turbulent flows such as channel flow, wake or plane jet. Although compact finite differences are extremely flexible in term of mesh generation and boundary conditions, geometries are restricted to computational domains which can be trivially mapped into the standard $[-1, 1]$ square. This restriction is well known in the context of spectral methods [2,3]. Multidomain methods were introduced to overcome this intrinsic limitation of spectral methods. A recent example of successful multidomain spectral method application is the computation of rotating flows in a T-shape geometry, carried out by Raspo [3]. Her study concerns a direct multidomain method in the vorticity stream function formulation of the two-dimensional Navier–Stokes equations. However, the extension of this formulation to three-dimensional flows is quite unsuitable.

In the context of the primitive variables formulation, the PDM was first introduced by Pinelli et al. [2]. It consists in solving each elliptic boundary value problems, deduced from the classical projection method of Kim and Moin [14], with a spectral multidomain method based on the weak formulation of the Steklov–Poincaré operator. Despite the remarkable accuracy of this spectral PDM, the large stencil of spectral methods is not suitable for complex flows and/or high aspect ratio geometries. In fact, a local singularity or unsuitable outflow conditions could lead to global numerical instabilities [15]. Instead of using spectral methods, high order finite differences may be an efficient alternative approach. They allow investigations of more realistic problems where mesh refinements are needed to describe local shears. Taking into account this feature, Danabasoglu et al. [1] adapted the original PDM of Pinelli et al. [2]. They derived a formulation based on a mixed fourth-order central difference/spectral method on a non-staggered mesh. Hence, they studied the flow over a step in a two-dimensional channel. However, as it was outlined by Morinishi et al. [16], the fourth-order central difference defined on a non-staggered mesh is not able to fulfill classical conservative properties, leading to unstable simulations of turbulent flows. In contrast, the fully staggered arrangement of Harlow and Welch [17] presents several advantages. The pressure–velocity coupling is made easier on a staggered grid. Indeed, Schiestel and Viazzo [8] reported that the discretization of the skew-symmetric formulation on a staggered grid conserves the kinetic energy and the momentum. Several works showed that spatial discretization of the Navier–Stokes equations on a staggered mesh with high order compact schemes is an efficient approach to simulate turbulent flows [6,8].

The purpose of the present work is to develop a two-dimensional PDM based on a fourth-order compact scheme defined on a fully staggered grid. The fourth-order compact schemes and staggered grid were chosen for their ability to simulate efficiently and accurately unsteady incompressible flows. The projection domain decomposition is selected to extend computations of numerical solutions of the Navier–Stokes equations on multi-connected rectangular domains. The strong formulation of Steklov–Poincaré operator is adopted to solve each elliptic solver resulting of the projection method. Moreover, the Poisson–Neumann problem is explicitly cleared-up without resorting to the capacitance matrix method unlike Danabasoglu et al. [1]. In the present paper, only a two-dimensional version of the compact scheme PDM is presented. If periodicity is assumed in one direction, the three-dimensional extension is possible by using Fourier series expansion in the periodic direction [2].

The organization of the paper is as follows. Section 2 describes the numerical method. The projection method and spatial discretization of the Navier–Stokes equations are firstly given. Then, the multidomain method for solving each Helmholtz/Poisson problem is presented. Finally, the first part is closed by a discussion on the solvability of the Poisson–Neumann problem. The second part is devoted to present the numerical results. The accuracy test results are shown and classical steady two-dimensional benchmark problems, such as the lid-driven cavity or the backward-facing step flow are investigated. The last section focuses on the flow over a square prism.

2. Numerical method

2.1. Single domain approach

The governing equations for an incompressible fluid flow are:

$$\begin{aligned} &\mathbf{u}_t + (\mathbf{u}\,.\,\nabla)\mathbf{u} = -\nabla p + \tfrac{1}{Re}\nabla^2\mathbf{u} && \text{in } \Omega,\\ &\nabla\,.\,\mathbf{u} = 0 && \text{in } \Omega, \end{aligned} \tag{1}$$

where $\mathbf{u}(\mathbf{x}, t)$ and $p(\mathbf{x}, t)$ are, respectively, the velocity vector and the static pressure. The Navier–Stokes equations are defined on a domain denoted Ω limited by a boundary noted $\partial\Omega$. All variables are non-dimensionalized by a characteristic velocity and length scale, and Re is the Reynolds number. The integration method used to solve Eq. (1) is based on a semi-implicit fractional step scheme [14]. The convective terms are advanced in time by using the explicit Adams–Bashforth scheme whereas the diffusive terms are advanced in time with the implicit Crank–Nicolson scheme. The resulting time discretized Navier–Stokes equations are:

$$\begin{aligned} &\tfrac{1}{\Delta t}(\mathbf{u}^{n+1} - \mathbf{u}^n) + \nabla p^{n+1/2} = \tfrac{3}{2}\mathcal{N}(\mathbf{u}^n) + \tfrac{1}{2}\mathcal{N}(\mathbf{u}^{n-1}) + \tfrac{1}{2Re}\nabla^2(\mathbf{u}^{n+1} + \mathbf{u}^n) && \text{in } \Omega,\\ &\nabla\,.\,\mathbf{u}^{n+1} = 0 && \text{in } \Omega. \end{aligned} \tag{2}$$

This semi-discrete form ensures a second-order time accuracy. In most DNS and LES applications, a wide variety of projection methods are often used to solve Eq. (2). Projection methods consist in decoupling pressure from velocity by solving firstly a provisional velocity and then an elliptic step to enforce the free divergence constraint. In this work the projection scheme of Kim and Moin [14] was selected. It is composed of three stages. First, the provisional field $\mathbf{u}^*$ is determined by solving:

$$\begin{aligned} &\frac{1}{\Delta t}(\mathbf{u}^* - \mathbf{u}^n) = \frac{3}{2}\mathcal{N}(\mathbf{u}^n) + \frac{1}{2}\mathcal{N}(\mathbf{u}^{n-1}) + \frac{1}{2Re}\nabla^2(\mathbf{u}^* + \mathbf{u}^n),\\ &\mathbf{n}\cdot\mathbf{u}^*|_{\partial\Omega} = \mathbf{n}\cdot\mathbf{u}^{n+1}|_{\partial\Omega},\\ &\boldsymbol{\tau}\,.\,\mathbf{u}^*|_{\partial\Omega} = \boldsymbol{\tau}\cdot(\mathbf{u}^{n+1} + \Delta t\nabla\phi^n)|_{\partial\Omega}. \end{aligned} \tag{3}$$

Then, a projection stage is performed to ensure the incompressibility condition

$$\begin{aligned} &\mathbf{u}^{n+1} = \mathbf{u}^* - \Delta t\nabla\phi^{n+1},\\ &\nabla\cdot\mathbf{u}^{n+1} = 0. \end{aligned} \tag{4}$$

The modified pressure ϕ^{n+1} is related by the following Poisson–Neumann system:

$$\begin{aligned} &\nabla\cdot\nabla\phi^{n+1} = \frac{\nabla\cdot\mathbf{u}^*}{\Delta t},\\ &\left.\frac{\partial\phi^{n+1}}{\partial n}\right|_{\partial\Omega} = 0. \end{aligned} \tag{5}$$

The final stage is the pressure updated from the modified pressure ϕ^{n+1}

$$p^{n+1/2} = \phi^{n+1} - \frac{\Delta t}{2Re}\nabla^2\phi^{n+1}. \tag{6}$$

The latter optional stage is performed to retrieve the pressure. This projection scheme was chosen because of its advantages. Indeed, the absence of the pressure gradient term in the momentum equation for $\mathbf{u}^*$ prohibits error in the pressure gradient, which could accumulate in time [18]. This error could be particularly prejudicial at the interfaces in the multidomain framework. According to discussions from different authors, this projection scheme ensures second-order time accuracy for the velocity. Concerning the temporal accuracy of the pressure, only first-order behavior was observed as in [18]. Several derived forms of this projection method allow more accurate prediction of the pressure variable. Eventually, the Kim and Moin scheme is selected for its robustness and its simplicity. Since convective terms are explicitly advanced in time, the projection method leads to Helmholtz and Poisson–Neumann problem for each flow variable Φ (i.e., u^*, v^*, ϕ):

$$\begin{aligned} &\Delta\Phi - \kappa\Phi = S \quad \text{in } \Omega, \\ &B\Phi = g \qquad\quad \text{on } \partial\Omega, \end{aligned} \tag{7}$$

where $\kappa = \Delta t/(2Re)$ for the provisional momentum equations and $\kappa = 0$ for the Poisson–Neumann problem. The boundary conditions are defined by the operator B.

The variable disposition chosen in the present work is the standard fully staggered cartesian grid. It prevents oscillatory numerical wiggles in the pressure field. Moreover, staggered grids associated with compact schemes have shown some good capabilities to describe turbulent fluid flows [8,16].

The approximation of variable derivatives is derived from compact schemes described by Lele in [4]. This implicit formulation exhibits very favorable accuracy and resolution properties with fewer stencil points in contrast with central finite differences. In this work, fourth-order compact scheme operators (see Appendix A) are rewritten, in such a way that derivative or interpolation of the variables are evaluated with a simple matrix–matrix product. This choice was motivated to make easier future extensions of the present method to sixth or higher order [4]. Hence, the following convenient discrete form of the two-dimensional discrete Helmholtz problem may be formulated as [19]:

$$\delta_{xx}\Phi + \Phi\delta_{yy} - \kappa\Phi = S, \tag{8}$$

where δ_{xx} and δ_{yy} are square matrices, related to the second derivative operators, Φ and S are matrices with dimension $n_x \times n_y$, respectively, associated with the unknowns and with the right-hand side of the Helmholtz problem (7). Hence, taking into account the boundary conditions for eliminating boundary nodes of Eq. (7) (see Appendix B), the discrete Helmholtz problem may be written as:

$$\delta^*_{xx}\Phi + \Phi\delta^*_{yy} - \kappa\Phi = S^*. \tag{9}$$

The superscript $*$ refers to modified matrices deduced by eliminating boundary nodes. Diagonalization technique is used to solve Eq. (9): the discrete problem is reformulated in the eigenvectors span, deduced from diagonalization of δ^*_{xx} and δ^*_{yy}. In fact, if diagonalizable properties of the matrices δ^*_{xx} and δ^*_{yy} are assumed, from $\Lambda_x = M_x^{-1}\delta^*_{xx}M_x$ and $\Lambda_y = M_y^{-1}\delta^*_{yy}M_y$ with Λ_x, Λ_y the diagonal matrices, and with M_x, M_y the matrices of the eigenvectors, one gets:

$$\Lambda_x\tilde{\Phi} + \tilde{\Phi}\Lambda_y - \kappa\tilde{\Phi} = \tilde{S}, \tag{10}$$

where $\tilde{\Phi} = M_x^{-1}\Phi M_y$ and $\tilde{S} = M_x^{-1}S^*M_y$. This yields:

$$\tilde{\Phi}_{ij} = \frac{\tilde{S}_{ij}}{\lambda_i^x + \lambda_j^y - \kappa}, \quad 2 < i < n_x - 1, 2 < j < n_y - 1 \tag{11}$$

with λ_i^x and λ_j^y the eigenvalues of the matrices δ_{xx}^* and δ_{yy}^*. Thus, the variable Φ is evaluated from $\Phi = M_x \tilde{\Phi} M_y$. The diagonalization technique is a powerful tool in term of cpu-time cost, since the solution computation requires only simple matrix–matrix products (the diagonalization of each modified operator is carried out only once during the preprocessing stage). It is a real advantage if computations are performed on vectorial architectures.

The eigenvalues were found always negative and real. However, mapping transformations involving too strong grid stretching could entail to complex eigenvalues. In this case, computation is given up because the cpu-time increases excessively. It should be noted that strong grid stretching could reduce the spatial accuracy [20]. Here, the loss of accuracy is minimized by using smooth coordinate mapping transform only. The matter is outlined in the numerical experiments section. In the context of momentum equations, this method does not involve particular difficulty since the denominator is never equal to zero. However, in the context of the singular Poisson–Neumann problem, a difficulty arises since the denominator may vanish: indeed, Neumann boundary conditions cancel one eigenvalue per direction. In this case, the solvability of the problem depends on the validity of the compatibility condition. In the favorable case, the compatibility condition is fulfilled and the problem admits a solution up to a constant. If the compatibility condition is violated, the Poisson–Neumann problem is not solvable. This property is intrinsic to the discrete spatial operators and will be discussed more precisely in Section 2.2.3.

2.2. Multidomain Helmholtz solver

2.2.1. Continuous formulation

The projection method reduces the time discretized Navier–Stokes equations into a set of Helmholtz and Poisson–Neumann problems. A convenient way to compute solutions of these problems in complex geometries is the multidomain method. This approach permits the substitution of the global Helmholtz problem defined in Ω by a set of K *sub-problems* on a non-overlapped partition $(\Omega_k)_{k=1,K}$ of Ω. These problems are coupled by prescribing continuity conditions of the variables and its normal derivatives across interfaces between each subdomain. These requirements, called *transmission conditions* [21], can be written as:

$$\frac{\partial \Phi_i}{\partial n} = \frac{\partial \Phi_j}{\partial n} \quad \text{and} \quad \Phi_i = \Phi_j \quad \text{for} \quad \partial\Omega_i \cap \partial\Omega_j. \tag{12}$$

These transmission conditions must be fulfilled on each point of the interface. In this section, a countable set of points $\{\gamma_{ik}\}_{k=1,\ldots,K_i}$, located on the interface, are introduced without lack of generality (see Fig. 1).

Before describing the method in details, some descriptions are given about notations those are further used in this section:

- Ω_i is a subdomain among the partition $(\Omega_k)_{k=1,K}$ of Ω.
- Γ_{ij} is the interface between subdomains Ω_i and Ω_j.
- Υ_i is the union of the interfaces of the subdomain Ω_i, and $\{\gamma_{ik}\}_{k=1,\ldots,K_i}$ are the nodes located on Υ_i.
- χ_i corresponds to the boundary of the subdomain Ω_i excluding its interface: $\chi_i = \partial\Omega_i/\Upsilon_i$.

Let us consider, in each subdomain, a solution of the linear problem (7) which is searched as the following linear combination:

$$\Phi_i = \tilde{\Phi}_i + \sum_{k=1}^{K_i} \lambda_{ik} \bar{\Phi}_{ik} \quad \text{in} \quad \Omega_i, \tag{13}$$

where $\tilde{\Phi}_i$ and $\bar{\Phi}_{ik}$ are, respectively, the solution of the two following problems:

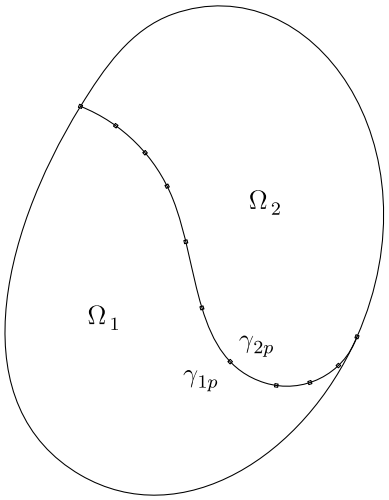

Fig. 1. An example of domain partition.

$$\begin{aligned} &\Delta\tilde{\Phi}_i - \kappa\tilde{\Phi}_i = S|_{\Omega_i} && \text{in } \Omega_i,\\ &B_i\tilde{\Phi}_i = g|_{\chi_i} && \text{on } \chi_i,\\ &\tilde{\Phi}_i = 0 && \text{on } \Upsilon_i \end{aligned} \tag{14}$$

and

$$\begin{aligned} &\Delta\bar{\Phi}_{ik} - \kappa\bar{\Phi}_{ik} = 0 && \text{in } \Omega_i,\\ &B_i\bar{\Phi}_{ik} = 0 && \text{on } \chi_i,\\ &\bar{\Phi}_{ik}(\gamma_{ip}) = \delta_{ip} && \text{for } \gamma_{ip} \in \Upsilon_i. \end{aligned} \tag{15}$$

The K_i functions $\bar{\Phi}_{ik}$ associated with the subdomain Ω_i are called *harmonic extensions* into Ω_i. Each function $\tilde{\Phi}_i$ defined to be solution of Eq. (14) is called *homogeneous solution*. In the previous linear combination, the coefficients λ_{ik} are obviously related to values of the whole solution Φ onto nodes belonging to the interfaces. From Eqs. (13)–(15), it may be stated that:

$$\lambda_{ip} = \Phi_i(\gamma_{ip}) \quad \text{for} \quad \gamma_{ip} \in \Upsilon_i. \tag{16}$$

From the transmission conditions, Eq. (12) applied to the linear combination Eq. (13), for two adjacent subdomains Ω_i and Ω_j yields:

$$\left(\frac{\partial\tilde{\Phi}i}{\partial n} + \sum_{k=1}^{K_i}\lambda_{ik}\frac{\partial\bar{\Phi}_{ik}}{\partial n}\right)\Bigg|_{\gamma_{ip}} = \left(\frac{\partial\tilde{\Phi}_j}{\partial n} + \sum_{k=1}^{K_j}\lambda_{jk}\frac{\partial\bar{\Phi}_{jk}}{\partial n}\right)\Bigg|_{\gamma_{jp}} \quad \text{with} \quad \gamma_{ip} = \gamma_{jp} \in \Upsilon_i \cap \Upsilon_j. \tag{17}$$

The latter equation, called Steklov–Poincaré equation, may be recasted in the following convenient form

$$\frac{\partial\tilde{\Phi}_i}{\partial n}(\gamma_{ip}) - \frac{\partial\tilde{\Phi}_j}{\partial n}(\gamma_{jp}) = \sum_{k=1}^{K_j}\lambda_k\left[\frac{\partial\bar{\Phi}_{jk}}{\partial n}(\gamma_{jp}) - \frac{\partial\bar{\Phi}_{ik}}{\partial n}(\gamma_{ip})\right] \quad \text{with} \quad \gamma_{ip} = \gamma_{jp} \in \Upsilon_i \cap \Upsilon_j. \tag{18}$$

The former relations written for each node belonging to the interfaces give K linear equations in which λ_k are the unknowns. Written in matrix notation, Eq. (18) may be expressed as follows:

$$\Xi\Lambda = H, \tag{19}$$

where Λ is the column vector of the interface unknowns. The matrix Ξ, called continuity influence matrix (CIM) by Raspo [3], represents a discretized formulation of the Steklov–Poincaré equation in the context of linear partial differential boundary values. It is obvious from Eq. (15) that the CIM depends only on the definition of the Helmholtz operator and on its kind of boundary conditions (Dirichlet, Neumann or Robin). The column vector H depends on the right-hand side F of the Eq. (14) and on its boundary values g. The next section, shows how this theoretical framework of the multidomain method is used in the discrete level.

2.2.2. Discrete formulation

In the former section, the multidomain method was recasted in a convenient continuous formulation. In the present section, the discrete formulation of the multidomain method is considered. For convenience and without lack of generality, we focus on the Poisson problem defined on a rectangular domain split into two rectangular non-overlapped subdomains (the extension to the Helmholtz problem is quite similar). The node distribution chosen hereafter is the variable pressure layout corresponding to the Poisson–Neumann problem. A sketch of the geometry and the arrangement of variables in the interface vicinity are depicted in Fig. 2.

The reduction of the multidomain continuous formulation into its discrete form is based on the set of transmission conditions in Eq. (18) applied to each node belonging to the interface. Indeed, this relation relates the interface unknowns as a function of the homogeneous solution $\tilde{\Phi}_i$ and the set of harmonic extensions $\bar{\Phi}_{ip}$ defined on each node belonging to the interfaces. Thus, after the spatial discretization of each subdomain, the numerical procedure is straightforward: it is sufficient to compute the CIM from each harmonic extensions, and then to clear up the interface values from each homogeneous solution and the CIM.

The numerical procedure is presented below in the present illustrative case, in which it is assumed that the two subdomains Ω_1 and Ω_2 are discretized using, respectively, $n_{1x} \times n_{1y}$ and $n_{2x} \times n_{2y}$ nodes. In that manner, the whole set of spatial compact operators is introduced. For example, δ_{1x}^{pu} and δ_{2x}^{pu} are the derivative operators defined on the staggered grid and, respectively, associated with the subdomains Ω_1 and Ω_2. Definitions and notations of the compact operators are detailed in Appendix A. Moreover, the interface nodes of Ω_1 must have the same location as the interface nodes of Ω_2: that implies $n_{1y} = n_{2y}$ (see Fig. 2). In this case the numerical multidomain procedure starts by initializing the Helmholtz solver on each subdomain, like in the single domain approach (see Section 2.1 and Appendix B). Thus, the discrete definition of each Poisson solver permits to compute each harmonic extension associated with each node belonging to the interface:

$$\begin{aligned} &\tfrac{\partial^2}{\partial x^2}\bar{\Phi}_{ik} + \tfrac{\partial^2}{\partial y^2}\bar{\Phi}_{ik} = 0 && \text{in } \Omega_i, \\ &B_i\bar{\Phi}_{ik} = 0 && \text{on } \Gamma_i \\ &\bar{\Phi}_{ik}(\gamma_p) = \delta_{ip} && \text{for } \gamma_p \in \Upsilon_i. \end{aligned} \tag{20}$$

From this set of *harmonic extensions*, the jumps of normal derivative are evaluated on the node interfaces to construct the CIM. In the present illustrative case, which includes only one interface discretized in K nodes, this stage is given by:

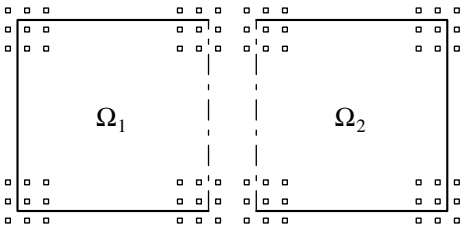

Fig. 2. Arrangement of pressure nodes at the corner and interface vicinities.

$$\Xi_{ij} = \left(\delta^{pu}_{1,x}\bar{\Phi}_{1i}\right)_{n_x-1/2,j} - \left(\delta^{pu}_{2,x}\bar{\Phi}_{2i}\right)_{3/2,j} \quad 1 \leqslant i, \quad j \leqslant K. \tag{21}$$

It may be noted that in the context of time discretized equations, each elliptic problem Eqs. (3) and (5) is time independent, and then harmonic extensions and the CIM are computed once and for all in the preprocessing stage.

Then, the problem defined on the whole domain is cleared up in the processing stages, which is composed of three internal stage. The first one, called the *first pass*, consists in solving the set of problems on each subdomain $i = 1,2$, with vanishing interface conditions:

$$\begin{aligned} &\tfrac{\partial^2}{\partial x^2}\tilde{\Phi}_i + \tfrac{\partial^2}{\partial y^2}\tilde{\Phi}_i = S|_{\Omega_i} && \text{in } \Omega_i, \\ &B_i\tilde{\Phi}_i = g|_{\Gamma_i} && \text{on } \Gamma_i, \\ &\tilde{\Phi}_i = 0 && \text{on } \Upsilon_i. \end{aligned} \tag{22}$$

From the previous homogeneous solutions, the column vector H can be computed. Herein, H is given by:

$$H_j = -\left(\delta^{pu}_{1,x}\tilde{\Phi}_1\right)_{n_x-1/2,j} + \left(\delta^{pu}_{2,x}\tilde{\Phi}_2\right)_{3/2,j} \quad 1 \leqslant j \leqslant K. \tag{23}$$

Then, the linear system which enforces the continuity of the first normal derivative through the interface, is solved to clear up the interface unknowns. This is achieved as follows:

$$\Lambda = \Xi^{-1}H, \tag{24}$$

where the CIM is inversed during the preprocessing stage. The direct method supplies the exact solution if one disregards rounding errors. The CIM inversion does not lead to any difficulty, except for the singular Poisson–Neumann problem in which some special attentions are needed. This point will be discussed in the next section.

Finally, after getting back the interface values, the whole solution is obtained by solving each problem defined on each subdomain Ω_i with the updated interface values:

$$\begin{aligned} &\tfrac{\partial^2}{\partial x^2}\Phi_i + \tfrac{\partial^2}{\partial y^2}\Phi_i = S|_{\Omega_i} && \text{in } \Omega_i, \\ &B\Phi_i = g|_{\Gamma_i} && \text{on } \Gamma_i, \\ &\Phi_i = \Lambda, && \text{on } \Upsilon_i. \end{aligned} \tag{25}$$

The former stage is called the *second pass*. Some properties on the continuity of the solutions obtained with the multidomain method need to be clarified. In fact, we postulated on the continuity of the Helmholtz solutions across the interface, through the transmission conditions in Eq. (12). Obviously, after discretizing each problem on the different subdomains, the previous transmission conditions have a meaning different from its continuous formulation. These conditions have to be interpreted in a discrete sense given by the considered discretized interpolation and derivation (see Appendix A).

So, because of the boundary conditions of each monodomain solver are prescribed for the second pass at the interfaces, the exact continuity (regardless rounding errors) of Φ across the interface is definitely satisfied. The continuity of the normal derivative across the interface depends directly on the accuracy of solving the linear system (19). This has mainly motivated the use of a direct method in the present work, all the more since no problem was observed on the conditioning of the CIM. This point will be discussed in the numerical experiments containing a large number of subdomains in Section 3.4.

As expected, the CIM inversion is not feasible for the singular Poisson–Neumann problem. The next section concentrates onto this problem in the projection method, since the singularity of this problem arises from the violation of the compatibility condition.

2.2.3. The Poisson–Neumann problem

The Poisson–Neumann problem defined by Eq. (5), is well known to be a singular problem. In practice, this essential difficulty is often overlooked, and a solution is found by iterative technique. Thus, a convergent solution cannot be found if the compatibility condition is not fulfilled [22]. In the framework of the multidomain method, the Poisson–Neumann problem was found to exhibit its singularity through the continuity influence matrix, and not through the discrete Poisson operators described in the monodomain section. Using the influence matrix method in order to enforce zero boundary divergence, Madabhushi et al. [23] observed a similar behaviour: the resulting influence matrix was singular. As suggested by Tuckerman [24], they constructed a modified influence matrix by replacing the null eigenvalues by any non-zero values. However, in the multidomain case, this regularization procedure leads to a discontinuous solution. In fact, as in the monodomain context, the problem is successfully cleared up by enforcing the compatibility condition of the Poisson–Neumann problem. This procedure is detailed hereafter. In the preprocessing stage, the CIM of the Poisson–Neumann problem has to be diagonalized:

$$\Xi = P^{-1} D P, \tag{26}$$

where D is the diagonal matrix, with a null value denoted by the index k_0, and P is the matrix containing the eigenvectors of Ξ. Thus, the solution of the linear system is straightforward since:

$$D_{kk}(P\Lambda)_k = (PH)_k \quad 1 \leqslant k \leqslant K. \tag{27}$$

However, since $D_{k_0 k_0} = 0$, the problem is only solvable if $(PH)_{k_0} = 0$. In this case, the problem admits a solution up to an arbitary additive constant, which is consistent with the physical nature of the pressure for incompressible flows. A sufficient condition for finding a solution is that the compatibility condition has to be fulfilled. This property is crucial for the projection decomposition domain. In fact, if the compatibility condition is not satisfied, the projection stage Eq. (4) is performed with a discontinuous gradient of the modified pressure ϕ (across the interfaces), leading to unsuitable discontinuity on the final velocity field.

In the present work, the derivative operators are based on fourth-order compact scheme described by Lele [4]. These schemes must be tuned to satisfy the compatibility condition in a discrete sense [4,6]. Instead of weighting the derivative operators with coefficients, a renormalization technique is preferred to enforce the mass flow balance on the provisional velocity field. This issue is motivated by the fact that the renormalization of the outflow is inevitable if convective conditions are used [30]. The outflow and inflow mass rate are evaluated with a quadrature formula compatible with the compact fourth-order discrete derivative δ^{pu} [25]. For this discrete derivative, the compatible quadrature formula is given by:

$$Q = \sum_{i=1}^{n} w_i f_i \tag{28}$$

with the weighting coefficients w_i:

$$\begin{aligned} w_1 &= w_n = 1, \\ w_2 &= w_{n-1} = \frac{13}{12}, \\ w_3 &= w_{n-2} = \frac{7}{8}, \\ w_4 &= w_{n-3} = \frac{25}{24}, \\ w_i &= 1 \quad 5 \leqslant i \leqslant n-4. \end{aligned} \tag{29}$$

3. Numerical experiments

The present section is devoted to assess the compact scheme PDM, which was previously presented. First, temporal and spatial accuracies of the compact scheme PDM are checked by comparison with an analytical solution of the Navier–Stokes equations (the decaying vortices). Then, three benchmark problems are investigated: the steady lid-driven cavity, the steady flow over a backward-facing step and the unsteady flow over a square prism. These three problems are chosen for their detailed description in the literature. Moreover, the flow past a square cylinder is a good challenge because of its unsteady vortex shedding.

3.1. Decaying vortices

In the following numerical experiments, we prove that the present compact scheme PDM does not deteriorate temporal and spatial accuracies. This objective is reached by matching the numerical solution with an analytical solution of the Navier–Stokes equations. The retained analytical solution is the unsteady flow of decaying vortices, namely:

$$\begin{aligned} u(x,y,t) &= -\exp(-2t\pi^2/Re)\cos(\pi x)\sin(\pi y),\\ v(x,y,t) &= \exp(-2t\pi^2/Re)\sin(\pi x)\cos(\pi y),\\ p(x,y,t) &= -\tfrac{1}{2}\exp(-4t\pi^2/Re)(\cos(\pi x)^2+\cos(\pi y)^2). \end{aligned} \tag{30}$$

Simulations are carried out in a square domain $-1 \leqslant x, y \leqslant 1$ which is partitioned in four square subdomains of unit length. Accuracy tests are performed with a Reynolds number fixed at $Re = 10$. This solution was also selected by previous authors [14,26] to test the accuracy of their numerical methods.

In the first part, we have reminded that the classical projection method of Kim and Moin ensures a second-order accuracy in time. To verify that the present compact schemes PDM retains the second-order accuracy in time, computations were performed using fine uniform mesh in both direction ($h = 1/58$). The maximum relative error in u, v and p at dimensionless time of 0.3 is plotted in Fig. 3 as function of

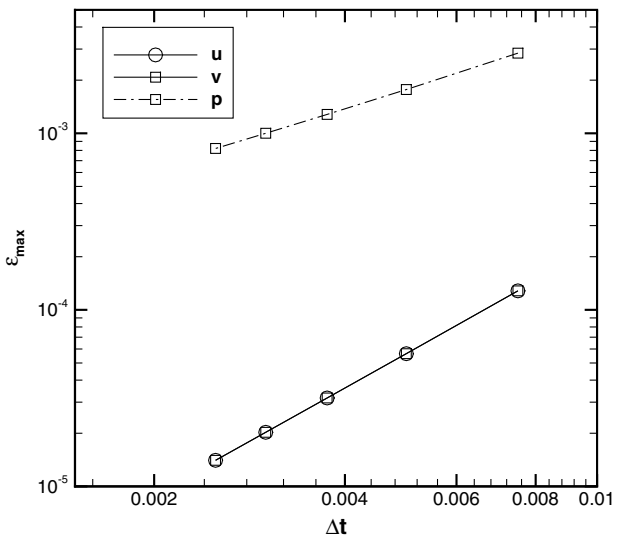

Fig. 3. Maximum relative error of the velocity components and the pressure as function of the time step.

the time step. As expected, Fig. 3 shows that the present method is truly second-order accurate in time for velocity variables.

For the pressure evaluated with Eq. (6), a first-order accuracy is observed. This behavior is in accordance with recent work of Brown et al. [18]. They proved, using the normal mode analysis, that the projection scheme of Kim and Moin is second-order for velocity and pressure, but in practice the pressure variable exhibits only a first-order accuracy.

The spatial accuracy is checked on both uniform and non-uniform meshes. With the uniform grid test, the maximum relative error is computed for different grid mesh spacings chosen over the range $\frac{1}{20} \leqslant h \leqslant \frac{1}{60}$. With the non-uniform grid test, the mesh is refined near the interfaces and close to the physical boundaries. The node distribution and the metrics are computed for each subdomain from the following coordinate transform mapping [30]:

$$y = \xi\left[\frac{1 - \tanh\gamma(\xi - \tilde{y})}{\tanh\gamma\xi}\right], \tag{31}$$

where the parameters γ and ξ control, respectively, the grid stretching and the inflexion point. These parameters are determined in such a way that the finest grid (located on each boundary) is set to $0.6h$, h being the uniform grid mesh spacing of the computational domain. In all computations, the time step is refined proportional to the grid spacing. The maximum relative error $\epsilon_{\max}$, for the flow variables u, v and p at the dimensionless time of 0.3, is plotted in Fig. 4 versus the mesh refinement.

Fig. 4 shows that the present method are indeed fourth-order accurate for all flow variables, and for both uniform and non-uniform grids.

In brief, the compact scheme PDM preserves the temporal accuracy of the projection scheme of Kim and Moin, as well as the spatial accuracy of the fourth-order compact scheme.

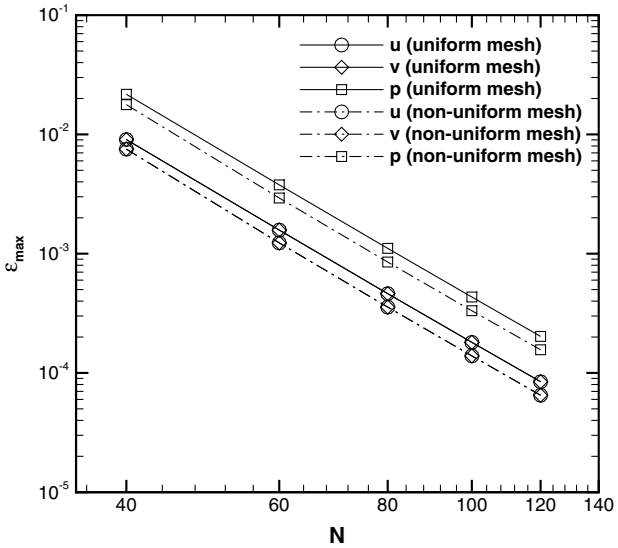

Fig. 4. Maximum relative error of the velocity components and the pressure as function of the mesh refinement.

3.2. The two-dimensional lid-driven cavity flow

The lid-driven flow in a two-dimensional cavity is among the well-established benchmark problem used to check the reliability of computational schemes. It was used by many authors and accurate solutions are available in the literature [27–29]. This problem consists in solving the Navier–Stokes equations in a unit square domain where the upper boundary moves with an uniform velocity ($u = 1, v = 0$). The no-slip boundary conditions are applied elsewhere ($u = 0, v = 0$). The domain is partitioned into four identical subdomains (see Fig. 5).

The grid sensitivity of the solution at the Reynolds number $Re = 400$ is achieved by performing different simulations where the uniform mesh grid spacing Δh is chosen among the following values: $\frac{1}{20}, \frac{1}{30}, \frac{1}{40}, \frac{1}{80}$ and $\frac{1}{130}$. The vertical velocity v versus the abscissa at mid-height ($y = 0.5$) and the horizontal velocity u versus the ordinate at $x = 0.5$ are plotted in Fig. 6.

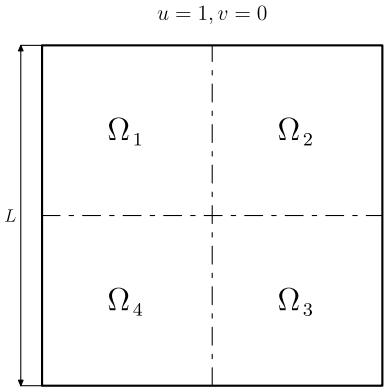

Fig. 5. Cavity flow: geometry and subdomains.

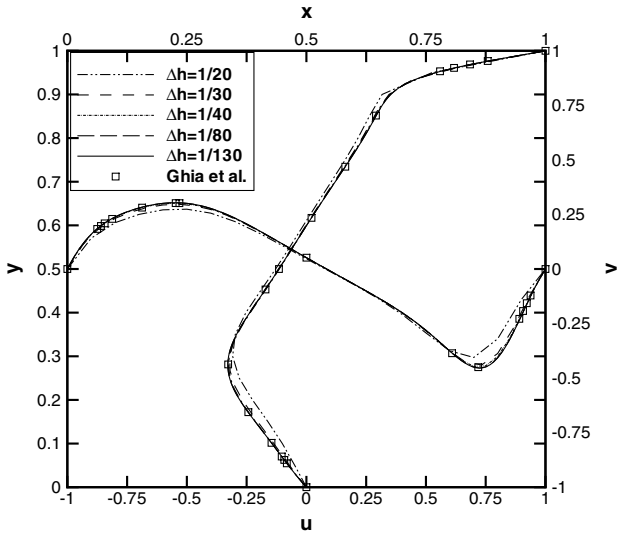

Fig. 6. Steady state velocity profiles in the lid-driven cavity at mid-height and mid-length ($Re = 400$).

The discrepancies between results obtained with grid mesh spacings beyond $\frac{1}{80}$ are not meaningful. Consequently, the lid-driven cavity flow solution shows a grid-independent character beyond a grid mesh spacing lower than $\frac{1}{80}$. It may be also concluded that our results are close to those obtained by Ghia et al. [27] when the grid mesh spacing is sufficiently small. Moreover, the values plotted in Fig. 6 are located on the interfaces of the partitioned domain (see Fig. 5). This shows the continuity properties through the interfaces are correctly treated. Streamlines and vorticity fields plotted in Fig. 7 match very well with the earlier investigations of Wan et al. [29].

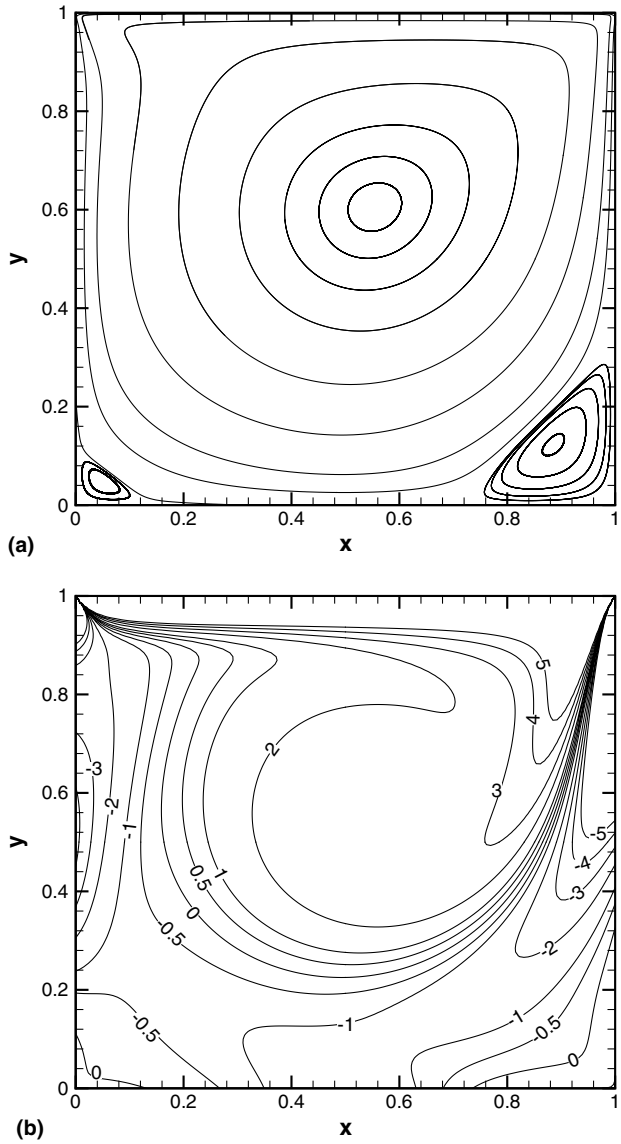

Fig. 7. Contour plots of streamline and vorticity for the lid-driven cavity flow. ($Re = 400$). (a) Streamlines. (b) Vorticity.

Two high Reynolds number computations were performed on the finest grid ($h = \frac{1}{130}$) for the Reynolds numbers $Re = 2500$ and $Re = 5000$ (see Fig. 8).

At these Reynolds numbers, the flow is still steady: Peng et al. [28] showed that unsteady pattern of the lid-driven cavity occurs with the first Hopf bifurcation at a Reynolds number $Re = 7402$. For the Reynolds numbers $Re = 2500$ and $Re = 5000$, the streamline plots are in accordance with the results of Wan et al. [29]. Four circulations occur: near the center of the cavity for the biggest circulation, and in both bottom corners. A small circulation can be also seen on the upper left side corner. It should be pointed out that no discontinuity occur on the primitive variables or on deduced variables like streamline or vorticity. That proves the robustness of the present compact scheme PDM.

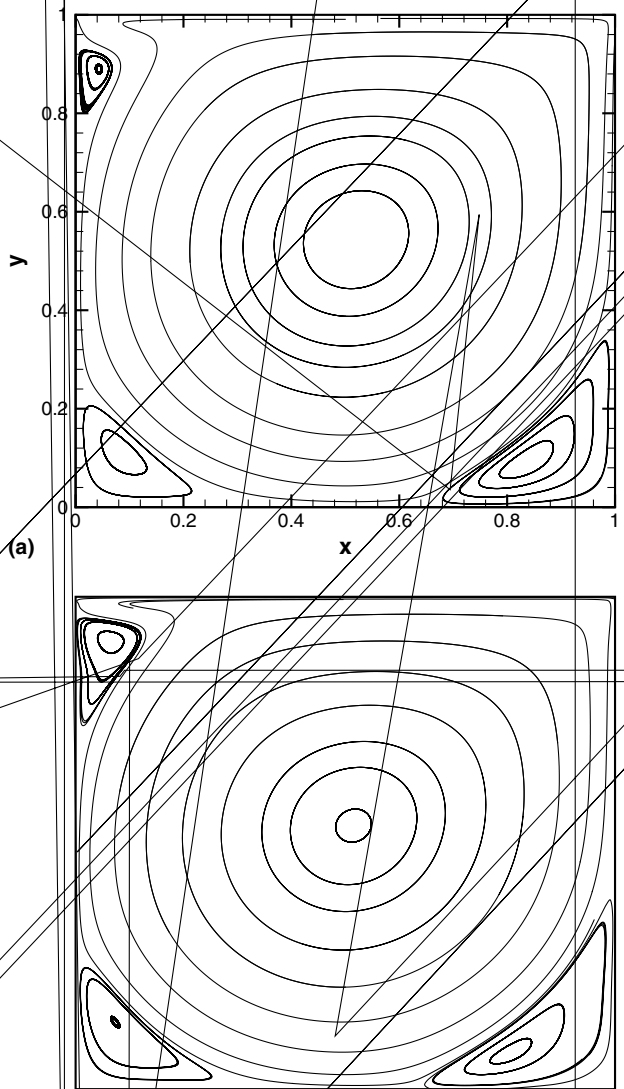

3.3. Flow over a backward-facing step

The former section was devoted to show the ability of the compact scheme PDM to compute accurately the solution of the lid-driven cavity. However, this benchmark seems tricky since exact mass balance is enforced within the boundary conditions. Thus, the compatibility condition is systematically fulfilled at each time step. In contrast, the flow over a backward facing step involves an outflow region, which is discretized with convective boundary conditions. Hence, this test case is a relevant problem to check the validity of the renormalization procedure described in the first part (Eq. 28).

The geometry of the domain and its partition are shown in Fig. 9.

By denoting h the step height, the upstream section have a length of $4h$ and a height of h. The height of the downstream channel is $2h$ and its length is $20h$. Thus, the selected expansion ratio is 2:1 allowing comparisons with the literature [29–31]. By denoting Re the Reynolds number based on the step height h and the averaged inlet velocity U_0, the reattachment length x_r (see Fig. 9) versus the Reynolds number Re is investigated over the range of 100–600. A wall boundary condition is imposed at the upper and lower boundaries, whereas parabolic and constant inlet profiles are prescribed in order to compare with some classical results [30,31] and more recent work [29].

The streamwise direction (ox) is uniformly discretized with 280 nodes resulting in a grid spacing of $\frac{3}{35}$. In the vertical direction, the mesh is refined near the step and close to the walls. The non-uniform grid is obtained from Eq. (31) with a uniform grid spacing fixed to $\frac{1}{50}$: the parameters γ and ξ are computed to set the finest grid at 0.009 close to the step and near the upper and lower walls. For the outflow region, a convective boundary condition is used to prescribe each component of the outflow velocity. This non-reflective boundary condition is based on the hyperbolic convection equation:

$$\frac{\partial u_i}{\partial t} + u_c \frac{\partial u_i}{\partial x} = 0, \tag{32}$$

where the convective velocity u_c is deduced from the bulk velocity. This boundary condition was successfully used by Le et al. [30]: they proved the numerical stability over the Reynolds number range 100–1000. However, if no special attention is paid, this non-reflective boundary condition leads to a violation of the compatibility condition which could be overcome with the tuned renormalization procedure previously developed in Section 2.2.3. It should be pointed out, that without the renormalization procedure, the Poisson–Neumann problem is anyway not correctly solved, leading to a discontinuous velocity field at the interfaces.

Streamlines of few selected Reynolds numbers are depicted in both Figs. 10 and 11.

Fig. 10 corresponds to the parabolic inlet profile whereas the second Fig. 11, corresponds to the constant inlet profile. The flow topology is fairly similar for both prescribed inlet conditions. However, some discrepancies may be noted on the reattachment lengths of the primary circulation. In fact, as it is shown in Table 1, the reattachment lengths for the parabolic inlet case are much higher than the constant inlet case.

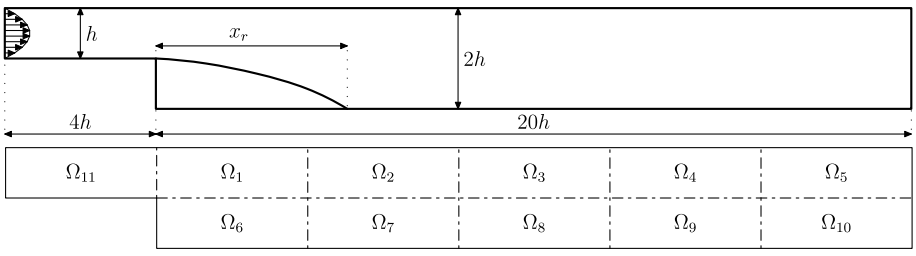

Fig. 9. Flow over a backward-facing step: geometry and partition.

[redacted]

The reattachment lengths versus the Reynolds number, obtained from the present compact scheme P[illegible]M, are [illegible] Fig. 12.

Some results of the literature [29–31] are also plotted, allowing quantitative comparisons. If the parabolic profile is prescribed, the reattachment lengths curve is contained between experimental results of Kimaly et al. [31] and numerical solutions of Le et al. [30]. The bad fitting between experimental results of Kimaly et al. [31] and numerical solutions can be explained with the well understood three-dimensional effects of the experiments. The reattachment lengths obtained with the numerical procedure of Le

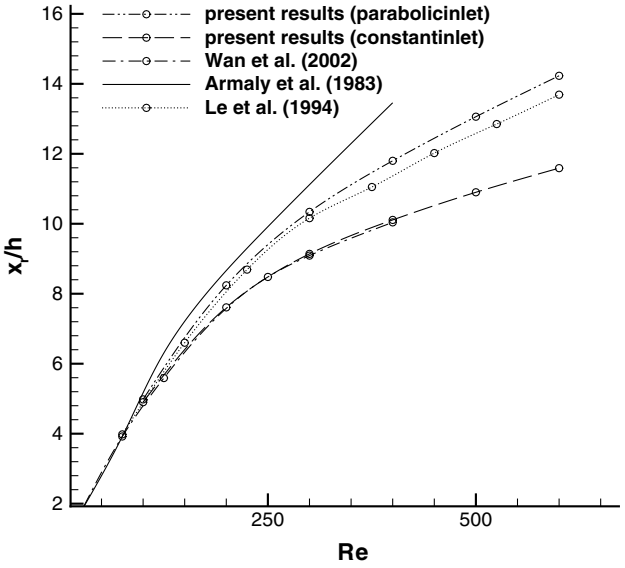

Fig. 12. Reattachment length versus the Reynolds number.

et al. [30] agrees more with our results than those published in [31]. However, some significant differences between these results still remain which may be cleared up by the considered geometry. Indeed, Le et al. [30] considered a rectangular domain in contrast with the present geometry which includes the upstream section. Wan et al. [29] gave some results on a similar geometry, but with a constant inlet profile. As it is shown in Fig. 12, if a constant inlet profile is prescribed, our results are very close to those of [29].

3.4. Flow past a square prism

The flow around a square prism is investigated to assess the present compact scheme PDM in a more complex flow. This classical benchmark was retained because of the unsteady behavior of the solution which occurs when the Reynolds number is above a critical value in the range over 54–70 [32–34]. The selected geometry is similar to the one of Breuer et al. [32]: it is composed of a square cylinder with a diameter D centered inside a plane channel (height H) with a blockage ratio fixed at $B = 1/8$. The channel length is fixed to $L/D = 48$ and the inflow length to $l = L/4$ (Fig. 13). As in the previous benchmark case, convective boundary conditions are applied on the outflow boundary. The velocity inlet condition is a parabolic profile with the maximum velocity $u_{\max}$ and no-slip boundaries are applied on the surface of the square cylinder and both on upper and lower boundaries of the computational domain. The goal of the present simulations is not to study precisely the flow past a square cylinder, but only to test our numerical scheme. Consequently, we focus on the selected Reynolds number $Re = 100$. The interest results are the drag coefficient C_d and the Strouhal number $St = fD/u_{\max}$ that characterizes the vortex shedding frequency.

The whole domain is partitioned into 20 subdomains (see Fig. 13). The downstream channel is decomposed into several subdomains to tackle the high aspect ratio.

Computations were carried out on two different meshes summed up in Table 2. These meshes are refined near the walls of the square cylinder and both on upper and lower boundaries. The analytical mapping Eq. (31) is used to refine independently each subdomain grid near boundaries.

The present compact scheme PDM is based on a direct inversion of the CIM, and consequently its well-conditioning is a relevant question for large dimension problems. In order to demonstrate that the CIM is

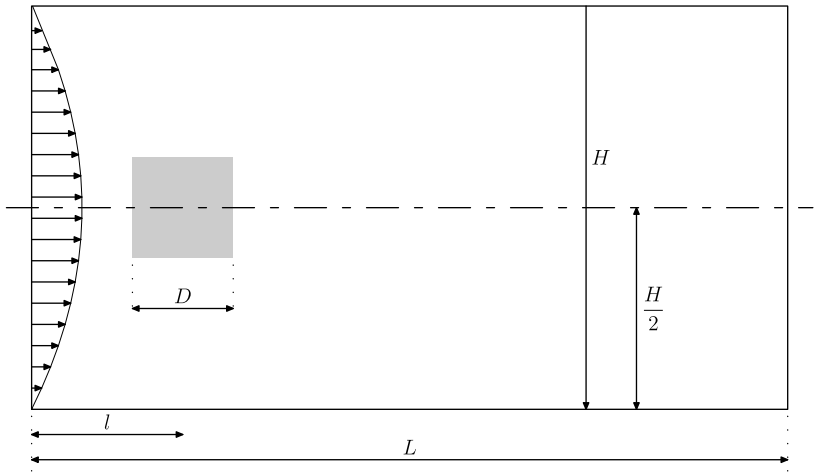

Ω_1	Ω_2	Ω_3	Ω_4	Ω_5	Ω_6	Ω_7
Ω_8		Ω_9	Ω_{10}	Ω_{11}	Ω_{12}	Ω_{13}
Ω_{14}	Ω_{15}	Ω_{16}	Ω_{17}	Ω_{18}	Ω_{19}	Ω_{20}

Fig. 13. Flow past a square cylinder: configuration and partition.

Table 2
Mesh size in each subdomain – nx_i and ny_j are, respectively, associated with the number of pressure node of the ith subdomain beginning from the inlet and the jth subdomain from the upper channel wall

	nx_1	nx_2	nx_3	nx_4	nx_5	nx_6	nx_7	ny_1	ny_2	ny_3
Mesh I	42	42	62	50	40	40	40	32	62	32
Mesh II	42	42	62	50	40	40	40	62	102	62

Table 3
Maximum jump of the normal derivative of the modified pressure versus the CIM pressure dimension

	CIM dimension	I_r
Mesh I	1124×1124	2.95×10^{-13}
Mesh II	1644×1644	5.69×10^{-13}

well-conditioned, the regularity of the modified pressure Φ is checked for each simulation. From Section 2.2.2, it is obvious that the regularity estimator I_r of the modified pressure is defined by the infinite norm of the jump of the normal derivative across each node belonging to the interfaces. Table 3 represents the maximum value of the jump during the two simulations versus the dimension of the CIM pressure for the two considered grids. The smallest range of the regularity estimator proves that the direct inversion of the Steklov–Poincaré system is correctly performed. Due to the well conditioning of the CIM, no significant effect of the subdomain ordering was observed on the solution. Hence, the use of compact schemes is a real advantage in comparison with spectral methods in which the conditioning of the CIM is severely

deteriorating with increasing the number of subdomains even if preconditioning techniques are applied [3]. The use of iterative solvers in the case of spectral methods with a large number of subdomains becomes inevitable but may be questionable in term of CPU time if spectral accuracy is nevertheless retained.

The temporal evolution of the vorticity and streamlines over one complete vortex shedding cycle of duration T is shown in Fig. 14.

Two-dimensional structures are formed behind the square, and then convected on the wake of the square prism. The visual sequence of vorticity shows the vortex generation phenomenon called Von Karman vortex street. It is interesting to observe that the domain partition does not disturb eddies transport phenomenon. Moreover, it should be pointed out the excellent vorticity behavior through the interfaces although no continuity constraint is directly prescribed on the vorticity variable. This last variable is computed from the velocity field and that confirms the robustness of the present domain decomposition method.

A quantitative description of the fluid flow feature is made by computing the drag coefficient C_d and the Strouhal number St. The drag coefficient is deduced from the integration of viscous and pressure strain acting on the square prism in the (ox) direction which are non-dimensionalized with the dynamic pressure $1/2\rho u_{max}^2$. The Strouhal number is defined by fD/u_{max}, in which the characteristic frequency f is determined by a spectral analysis of a time sample of the viscous drag. The power density spectrum is shown in Fig. 15.

For the fine and coarse meshes the Strouhal numbers and mean drag coefficient are identical, indicating that the grid independence character is reached for this value. These values are compared to the numerical

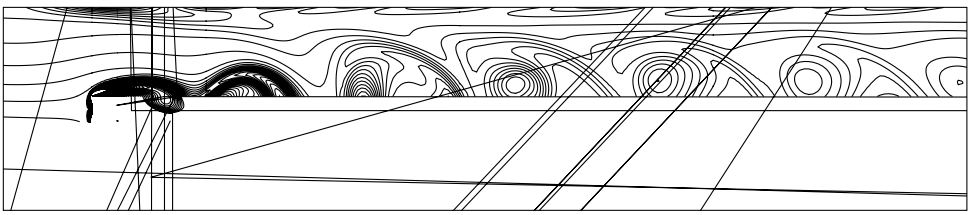

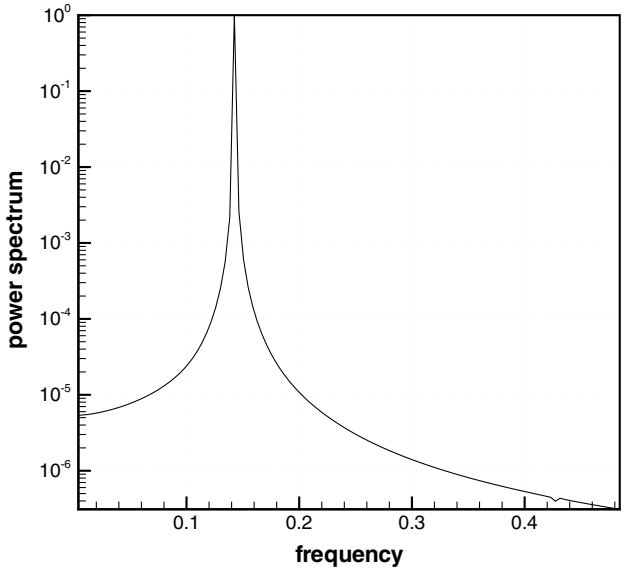

Fig. 15. Power spectrum of the time series of the viscous drag.

Table 4
Comparison of different physical parameters for flow past a square prism $Re = 100$

	C_d	St
Present study (grid I)	1.389	0.143
Present study (grid II)	1.388	0.143
Breuer et al. [32]	1.37	0.139

results of [32] (see Table 4), which were obtained by using lattice Boltzman and finite volumes discretizations. The Strouhal number obtained with the present study is slightly over-estimated in comparison with [32]. The mean drag coefficient is also close to the value given in [32]. This test shows the ability of the present method to deal with unsteady laminar flow.

4. Conclusion

A direct projection decomposition method based on a fourth-order compact scheme defined on a fully staggered grid was presented. The originality of the method lies in the differential formulation of each Helmholtz/Poisson multi-domain problem resulting of the classical Kim and Moin projection method. The difficult Poisson/Neumann problem was correctly resolved by enforcing the compatibility condition and using a diagonalization method of the continuity influence matrix. Moreover, since the flow variables are located on a fully staggered grid, the incompressibility constraint is exactly enforced in the whole inner domain. The present compact scheme PDM enables the computation of 2D laminar flows in geometries composed of multi-connected rectangular domains. This method possesses a strong potentiality for high performance computing: the non-iterative treatment of the transmission conditions would yield a true parallel algorithm, in which the time communications between processors will be reduced. Besides, in the numerical experiments, some detailed two-dimensional problems were solved to show the robustness and

the reliability of the present compact scheme PDM. Matching our results with an analytical solution of the Navier–Stokes equations showed that the compact scheme PDM preserves the expected theoretical accuracy of the temporal and spatial discretization. The classical lid-driven cavity flow was investigated and a good agreement was obtained with the literature. The validity of the renormalization procedure to ensure the compatibility condition was verified for the backward-facing step flow. Finally, the unsteady flow past a square prism proved that the interface discretization has not modified the vortex shedding as well as the well conditioning of the numerical method despite the large interface unknowns. That indicates the present compact scheme PDM is an accurate, reliable, and robust approach for dealing with incompressible two-dimensional laminar flows in geometries composed of multi-connected rectangular domains.

5. Future work

The two-dimensional formulation of the projection decomposition method was established and checked in this paper. Our aim being to simulate three-dimensional turbulent flows, the next stage will consist to the extension to a three-dimensional formulation. An obvious way would consist in discretizing the third direction as the two first. However, in this case, the CIM matrix dimension will rapidly increase and become too huge to be solved efficiently. In future work, only turbulent flows with one homogeneous direction will be considered by assuming a periodicity in this direction. This assumption allows the use of pseudo-spectral methods, and so, the three-dimensional problem will reduce to a series of two-dimensional problems associated with each wavenumber.

Acknowledgements

This work was supported by a Grant of the Région Pays de la Loire. We are also grateful to the Centre de Calcul Intensif des Pays de la Loire (CCIPL) and to the Institut du Développement et des Ressources en Informatique Scientifique (IDRIS) where the numerical simulations reported here were carried out.

Appendix A. Compact difference schemes

Compact difference schemes allow the discrete evaluation of derivative and interpolation operators. Their formulations are based on a set of implicit relations obtained with Taylor series expansion. To define the whole discrete operators which are used, we consider the typical discretization of the interval $[0,L_\xi]$ on a staggered grid. Thus, the velocity and pressure node locations are, respectively, defined by $\xi_{i+\frac{1}{2}} = (i-1)h$ and $\xi_i = (i-\frac{3}{2})h$, with the uniform grid spacing $h = \frac{L_\xi}{N_\xi - 2}$. All compact schemes can be expressed by the following set of linear algebraic equations:

$$Hf' = Af, \tag{A.1}$$

where each row represents an implicit relation between the derivatives and function values for computational nodes. These relations are described at the end of this appendix. These equations can also be written in an equivalent explicit form by

$$f' = H^{-1}Af = \delta_\xi f, \tag{A.2}$$

where δ_ξ is not necessarily compact. The notations δ_ξ^{uu}, δ_ξ^{pu} and δ_ξ^{up} correspond to the first derivative with respect to ξ, whereas $\imath_\xi^{pu}$ and $\imath_\xi^{up}$ are the discrete interpolation operators and $\delta_{\xi\xi}^{uu}$ is the second derivative with respect to ξ. The first superscript is associated with the node location of the known function and the second

Table A.1
Compact scheme coefficients

Schemes	Inner nodes		Boundary nodes				
	α	a	α	a	b	c	d
δ_ξ^{uu} (A.3)	$\frac{1}{4}$	$\frac{1}{4}$	2	$-\frac{5}{2}$	2	$\frac{1}{2}$	–
$\delta_{\xi\xi}^{uu}$ (A.8)	$\frac{1}{10}$	$\frac{1}{4}$	11	13	-27	15	-1
δ_ξ^{up} (A.4)	$\frac{1}{22}$	$\frac{12}{11}$	23	-25	26	-1	–
δ_ξ^{pu} (A.5)	$\frac{1}{22}$	$\frac{12}{11}$	23	-1	2	-1	–
ι_ξ^{pu} (A.6)	$\frac{1}{6}$	$\frac{2}{3}$	5	$\frac{15}{4}$	$\frac{5}{2}$	$-\frac{1}{4}$	–
ι_ξ^{up} (A.7)	$\frac{1}{6}$	$\frac{2}{3}$	1	$\frac{1}{4}$	$\frac{3}{2}$	$\frac{1}{4}$	–

refers to the unknown evaluation location. For example, δ_ξ^{pu} is the first derivative operator from pressure nodes toward velocity nodes. Hereafter, the implicit relations, defining each operator and including inner and boundary nodes, are described hereafter (the coefficients are itemized in Table A.1):

$$\delta_\xi^{uu}\begin{cases}\alpha f'_{i-1}+f'_i+\alpha f'_{i+1}=a\frac{f_{i+1}-f_{i-1}}{2h}\\ f'_1+\alpha f'_2=\frac{af_1+bf_2+cf_3}{h}\end{cases}, \tag{A.3}$$

$$\delta_\xi^{up}\begin{cases}\alpha f'_{i-1}+f'_i+\alpha f'_{i+1}=a\frac{f_{i+1/2}-f_{i-1/2}}{h}\\ f'_1+\alpha f'_2=\frac{af_{3/2}+bf_{5/2}+cf_{7/2}}{h}\end{cases}, \tag{A.4}$$

$$\delta_\xi^{pu}\begin{cases}\alpha f'_{i-1/2}+f'_{i+1/2}+\alpha f'_{i+3/2}=a\frac{f_{i+1}-f_i}{h}\\ f'_{3/2}+\alpha f'_{5/2}=\frac{af_1+bf_2+cf_3}{h}\end{cases}, \tag{A.5}$$

$$\iota_\xi^{up}\begin{cases}\alpha f_{i-1}+f_i+\alpha f_{i+1}=a(f_{i+1/2}-f_{i-1/2})\\ f_1+\alpha f_2=af_{3/2}+bf_{5/2}+cf_{7/2}\end{cases}, \tag{A.6}$$

$$\iota_\xi^{pu}\begin{cases}\alpha f_{i-1/2}+f_{i+1/2}+\alpha f'_{i+3/2}=a(f_{i+1}-f_i)\\ f_{3/2}+\alpha f_{5/2}=af_1+bf_2+cf_3\end{cases}, \tag{A.7}$$

$$\delta_{\xi\xi}^{uu}\begin{cases}\alpha f''_{i-1}+f''_i+\alpha f''_{i+1}=a\frac{f_{i+1}-2f_i+f_{i-1}}{h^2}\\ f''_1+\alpha f''_2=\frac{af_1+bf_2+cf_3+df_4}{h^2}\end{cases}. \tag{A.8}$$

Appendix B. Discrete formulation of the Helmholtz/Poisson problem

This appendix describes in details the methodology used to formulate the discrete Helmholtz/Poisson problem with compact scheme discretizations. We focus on the discrete Poisson–Neumann problem defined on one subdomain. The spatial discretization of the modified pressure equation (7) on the pressure grid yields:

$$\sum_{l=1}^{n_x}\beta_{il}^x\Phi_{l,j}+\sum_{n=1}^{n_y}\beta_{jn}^y\Phi_{i,n}=S_{i,j}, \tag{B.1}$$

where the discrete operators associated with the second derivative in each direction are defined by

$$\beta^x_{il} = \sum_{q=1}^{n_x-1} \delta^{up}_{x,iq}\delta^{pu}_{x,ql},$$
$$\beta^y_{jn} = \sum_{q=1}^{n_y-1} \delta^{up}_{y,jq}\delta^{pu}_{y,qn}. \tag{B.2}$$

In the case of homogeneous Neumann boundary conditions, boundary nodes can be expressed as function of inner nodes:

$$\begin{aligned}
\Phi_{1,j} &= \sigma^x_{1n_x}\sum_{i=2}^{n_x-1}\delta^{pu}_{n_x i}\Phi_{i,j} + \sigma^x_{n_xn_x}\sum_{i=2}^{n_x-1}\delta^{pu}_{1i}\Phi_{i,j},\\
\Phi_{1,j} &= \sigma^x_{1n_x}\sum_{i=2}^{n_x-1}\delta^{pu}_{n_x i}\Phi_{i,j} + \sigma^x_{n_xn_x}\sum_{i=2}^{n_x-1}\delta^{pu}_{1i}\Phi_{i,j},\\
\Phi_{i,1} &= \sigma^y_{1n_y}\sum_{j=2}^{n_y-1}\delta^{pu}_{n_y j}\Phi_{i,j} + \sigma^y_{n_yn_y}\sum_{j=2}^{n_y-1}\delta^{pu}_{1j}\Phi_{i,j},\\
\Phi_{i,n_y} &= \sigma^y_{11}\sum_{j=2}^{n_y-1}\delta^{pu}_{n_y j}\Phi_{i,j} + \sigma^y_{n_y1}\sum_{j=2}^{n_y-1}\delta^{pu}_{1j}\Phi_{i,j},
\end{aligned} \tag{B.3}$$

where

$$\begin{aligned}
\sigma^x_{11} &= \frac{\delta^{pu}_{11}}{\delta^{pu}_{n_x1}\delta^{pu}_{1n_x} - \delta^{pu}_{n_xn_x}\delta^{pu}_{11}}, \quad \sigma^x_{1n_x} = \frac{-\delta^{pu}_{1n_x}}{\delta^{pu}_{n_x1}\delta^{pu}_{1n_x} - \delta^{pu}_{n_xn_x}\delta^{pu}_{11}},\\
\sigma^x_{n_x1} &= \frac{-\delta^{pu}_{n_x1}}{\delta^{pu}_{n_x1}\delta^{pu}_{1n_x} - \delta^{pu}_{n_xn_x}\delta^{pu}_{11}}, \quad \sigma^x_{n_xn_x} = \frac{\delta^{pu}_{n_xn_x}}{\delta^{pu}_{n_x1}\delta^{pu}_{1n_x} - \delta^{pu}_{n_xn_x}\delta^{pu}_{11}},\\
\sigma^y_{11} &= \frac{\delta^{pu}_{11}}{\delta^{pu}_{n_y1}\delta^{pu}_{1n_y} - \delta^{pu}_{n_yn_y}\delta^{pu}_{11}}, \quad \sigma^y_{1n_y} = \frac{-\delta^{pu}_{1n_y}}{\delta^{pu}_{n_y1}\delta^{pu}_{1n_y} - \delta^{pu}_{n_yn_y}\delta^{pu}_{11}},\\
\sigma^y_{n_y1} &= \frac{-\delta^{pu}_{n_y1}}{\delta^{pu}_{n_y1}\delta^{pu}_{1n_y} - \delta^{pu}_{n_yn_y}\delta^{pu}_{11}}, \quad \sigma^y_{n_yn_y} = \frac{\delta^{pu}_{n_yn_y}}{\delta^{pu}_{n_y1}\delta^{pu}_{1n_y} - \delta^{pu}_{n_yn_y}\delta^{pu}_{11}}.
\end{aligned} \tag{B.4}$$

Eliminating boundary nodes in Eq. (B.1) with the above relations, the system may be rewritten with only inner nodes:

$$\sum_{l=2}^{n_x-1}\omega^x_{il}\Phi_{l,j} + \sum_{n=2}^{n_y-1}\omega^y_{jn}\Phi_{i,n} = F_{i,j}, \tag{B.5}$$

where ω^x and ω^y are the modified operators defined by

$$\begin{aligned}
\omega^x_{il} &= \beta^x_{il} + \beta^x_{i1}\left(\sigma^x_{1n_x}\delta^{pu}_{n_xl} + \sigma^x_{n_xn_x}\delta^{pu}_{1l}\right) + \beta^x_{in_x}\left(\sigma^x_{11}\delta^{pu}_{n_xl} + \sigma^x_{n_x1}\delta^{pu}_{1l}\right),\\
\omega^y_{jn} &= \beta^y_{jn} + \beta^y_{j1}\left(\sigma^y_{1n_y}\delta^{pu}_{n_yn} + \sigma^y_{n_yn_y}\delta^{pu}_{1n}\right) + \beta^y_{jn_y}\left(\sigma^y_{11}\delta^{pu}_{n_yn} + \sigma^y_{n_y1}\delta^{pu}_{1n}\right).
\end{aligned} \tag{B.6}$$

Finally, the diagonalization stage is applied on the system Eq. (B.5) and the boundary nodes are recovered with Eq. (B.3).

References

[1] G. Danabasoglu, S. Biringen, C.L. Streett, Application of the spectral multidomain method to the Navier–Stokes equations, J. Comput. Phys. 113 (1994) 155–164.

[2] A. Pinelli, A. Vacca, A. Quarteroni, A spectral multidomain method for the numerical simulation of turbulent flows, J. Comput. Phys. 136 (1997) 546–558.
[3] I. Raspo, A direct spectral domain decomposition method for the computation of rotating flows in a T-shape geometry, Comput. Fluids 32 (2003) 431–456.
[4] S.K. Lele, Compact finite difference schemes with spectral-like resolution, J. Comput. Phys. 103 (1992) 16–42.
[5] J.W. Kim, D.J. Lee, Optimized compact finite difference schemes with maximum resolution, AIAA J. 345 (1996) 887–893.
[6] S. Nagarajan, S.K. Lele, J.H. Ferziger, A robust high-order compact method for large eddy simulation, J. Comput. Phys. 191 (2003) 392–419.
[7] J.M.C. Pereira, M.H. Kobayashi, J.C.F. Pereira, A fourth-order-accurate finite volume compact method for the incompressible Navier–Stokes solutions, J. Comput. Phys. 167 (2001) 217–243.
[8] R. Schiestel, S. Viazzo, A Hermitian-Fourier numerical method for solving the incompressible Navier–Stokes equations, Comput. Fluids 24 (1995) 739–752.
[9] S. Smirnov, C. Lacor, M. Baelmans, A finite volume formulation for compact scheme with applications to LES, AIAA Paper 2001-2546, in: 15th AIAA Computational Fluid Dynamics Conference, June 11–14, Anaheim, CA, 2001.
[10] D.V. Gaitonde, J.S. Shang, Optimized Compact-difference-based finite-volume schemes for linear wave phenomena, J. Comput. Phys. 138 (1997) 617–643.
[11] C. Lacor, S. Smirnov, M. Baelmans, A finite volume formulation of compact central schemes on arbitrary structured grids, J. Comput. Phys. 198 (2004) 535–566.
[12] M.R. Visbal, D.V. Gaitonde, High-order accurate methods for unsteady vortical flows on curvilinear meshes, AIAA Paper, 1998, pp. 98–131.
[13] M.R. Visbal, D.V. Gaitonde, On the use of higher-order finite-difference schemes on curvilinear and deforming meshes, J. Comput. Phys. 181 (2002) 155–185.
[14] J. Kim, P. Moin, Application of a fractional-step method to incompressible Navier–Stokes equations, J. Comput. Phys. 59 (1985) 308–323.
[15] F. Auteri, N. Parolini, L. Quartapelle, Numerical investigation on the stability of singular driven cavity flow, J. Comput. Phys. 183 (2002) 1–25.
[16] Y. Morinishi, T.S. Lund, O.V. Vasilyev, P. Moin, Fully conservative higher order finite difference schemes for incompressible flow, J. Comput. Phys. 143 (1998) 90–124.
[17] F.H. Harlow, J.E. Welch, Numerical calculation of time-dependent viscous incompressible flow of fluid with free surface, Phys. Fluids 812 (1965) 2182–2189.
[18] D.L. Brown, R. Cortez, M.L. Minion, Accurate projection methods for the incompressible Navier–Stokes equations, J. Comput .Phys. 168 (2001) 464–499.
[19] C. Canuto, M.Y. Hussaini, A. Quarteroni, T.A. Zang, Spectral Methods in Fluid Dynamics, Springer Verlag, Berlin, 1988.
[20] L. Gamet, F. Ducros, F. Nicoud, T. Poinsot, Compact finite difference schemes on non-uniform meshes. Application to direct numerical simulations of compressible flows, Int. J. Numer. Meth. Fluids 29 (2) (1999) 159–191.
[21] A. Quarteroni, A. Valli, Domain Decomposition Methods for Partial Differential Equations, Numerical Mathematics and Scientific Computation, Oxford Science Publications, Oxford, 1999.
[22] C. Pozrikidis, A note on the regularization of the discrete Poisson/Neumann problem, J. Comput. Phys. 172 (2001) 917–923.
[23] R.K. Madabhushi, S. Balachandar, S.P. Vanka, A divergence-free Chebyshev collocation procedure for incompressible flows with two non-periodic directions, J. Comput. Phys. 105 (1993) 199–206.
[24] L.S. Tuckerman, Divergence-free velocity fields in non-periodic geometries, J. Comput. Phys. 80 (1989) 403–441.
[25] E. Védy, S. Viazzo, R. Schiestel, A high-order finite differences method for incompressible fluid turbulence simulations, Int. J. Numer. Meth. Fluids 42 (11) (2003) 1155–1188.
[26] Y. Zang, R.L. Street, J.R. Koseff, A non-staggered grid fractional step method for time dependent incompressible Navier–Stokes equations in curvilinear coordinates, J. Comput. Phys. 114 (1994) 18–33.
[27] U. Ghia, K.N. Ghia, C.T. Shin, High-resolutions for incompressible flow using the Navier–Stokes equations and a multigrid method, J. Comput. Phys. 48 (1982) 387–411.
[28] Y.F. Peng, Y.H. Shiau, R.R. Hwang, Transition in a 2-D lid-driven cavity flow, Comput. Fluids 32 (2003) 337–352.
[29] D.C. Wan, B.S.V. Patnaik, G.W. Wei, Discrete singular convolution-finite subdomain method for the solution of incompressible viscous flow, J. Comput. Phys. 180 (2002) 229–255.
[30] H. Le, P. Moin, Direct numerical simulation of turbulent flow over a backward-facing step, Report TF-58, Thermosciences Division, Dept. of Mech. Eng. Stanford University, 1994.
[31] B.F. Armaly, F. Durst, J.C.F. Pereira, B. Schoung, Experimental and theoretical investigation of backward-facing step flow, J. Fluid Mech. 127 (1983) 473–496.
[32] M. Breuer, J. Bernsdorf, T. Zeiser, F. Durst, Accurate computations of the laminar flow past a square cylinder based on two different methods: lattice-Boltzmann and finite-volume, Int. J. Heat Fluid Flow 21 (2000) 186–196.

[33] A. Okajima, Strouhal numbers of rectangular cylinder, J. Fluid Mech. 123 (1982) 379–398.
[34] A. Okajima, Numerical simulation of flow around rectangular cylinder, J. Wind Eng. Ind. Aerodyn. 33 (1990) 171–180.